

The Effect of Deep Burial and Folding on Sandstone Reservoirs in some Giant Gas Fields, South America

Prof. Gregory Smith*

Department of Applied Geology,
Curtin University
GPO Box U1987, Perth, WA 6845
Gregory.c.smith@curtin.edu.au

Prof. Reza Rezee

Department of Petroleum Engineering,
Curtin University
GPO Box U1987, Perth WA 6845
R.Rezaee@curtin.edu.au

Prof. Maxim Lebedev

Department of Exploration Geophysics
Curtin University
GPO Box U1987, Perth WA 6845
M.Lebedev@curtin.edu.au

Assoc. Prof Stefan Iglauer

Department of Petroleum Engineering
Curtin University
GPO Box U1987, Perth WA 6845
Stefan.Iglauer@curtin.edu.au

*presenting author asterisked

SUMMARY

The underthrust fold belt of the Andes contains some very large gas fields in which the Lower Palaeozoic Sandstone reservoirs are buried to depths of over 4-6km. The foreland depositional environment received high amounts of metamorphic and igneous rock fragments and deep burial was accompanied by substantial tectonic folding and fracturing. The combined effects of Temperature, Pressure and time on these labile sediments have reduced typical porosities <7% and matrix permeabilities <1mD so that these reservoirs are ultra-tight and effectively unconventional. Nevertheless, the fields contain very large recoverable amounts of gas with minor liquids per well. They provide an intriguing case study that contrasts with the typical concept of a conventional petroleum sandstone prospect and pose the question how many more large gas fields fit this model?

These complex structural fields required modelling by 3D-Geo using fractured and folded simulation models. The micro-porosity and micro-permeability has been investigated by Curtin University using nano-scale special core analysis in an attempt to identify where the hydrocarbons reside in these rocks, how they migrate out on production, and how best to estimate and optimize ultimate recovery?

High technology characterization included TIMA-SEM to map mineralogy and texture at the nano-scale; X-ray Micro-CT analysis of 3D microstructure; NMR, ultra-low Helium porosity and permeability, Hg injection for capillary pressure; Elastic and Electrical Properties to tie the seismic and log data for the modelling. Tri-axial tests helped understand the structural and tectonic history and its relation to the burial history of the reservoirs.

Key words: underthrust fold traps, fractured sandstones, ultra-tight sandstones, nano-scale reservoir analysis.

1.0 INTRODUCTION

A series of very large hydrocarbon fields occur within the eastern Andean Fold Belt in South America (Figure 1). The folds outcrop at the surface whereas the mainly gas-bearing reservoirs occur in complex traps within thrust or under-thrust folds at some 4-6km depth (Moretti *et al.*, 1996). The sandstones have been subjected to deeper burial and have been uplifted by subsequent thrust folding. Consequently, they are ultra-tight reservoirs with very low porosities (typically 0.5-7%) and very low permeabilities (typically 0.0001-1mD matrix permeability) so that normally they would not be expected to form economic petroleum fields. However, the thrust faulting and folding have produced an extensive fracture network at various scales. The fractures that occur in core have been analysed for frequency, size, porosity and permeability with the latter indicating permeabilities up to and over 1Darcy.

The structure of these folds has been studied in detail based on outcrop traverses (Florez-Nino *et al.*, 2005) and the traps are considered compartmentalised by the large faults (Moretti *et al.*, 2002) which is consistent with their production behaviour. Some burial history studies have been made (Baby *et al.*, 1995; Moretti *et al.*, 1996) that concluded the Devonian marine source rocks had been buried prior to uplift in the Permian to Jurassic, followed by a second phase of deep burial associated with the Andean deformation and cover by Tertiary sediments. Miranda *et al.* (2003) have provided a sequence stratigraphic framework for the Devonian reservoirs. The reservoir quality has been assessed with extensive traditional core analysis by the operating petroleum companies for each field though very little of this data has been published or interpreted as an integrated dataset. Hence, many questions remain for these ultra-tight but fractured reservoirs in terms of the reservoir character and its control on hydrocarbon volumes and recovery. Reserve estimates are equivocal given it is not clear whether the gas resides in micropores connected to the fractures or only in the fractures for which accurate pore volumes is uncertain. Production from the gas fields commonly experiences rapid drop-off from peak with early water ingress. Existing reservoir characterization and petrophysical studies have assumed a low wetting phase irreducible saturation that results in low connate water saturation (S_w) when the laboratory capillary pressures are converted to reservoir conditions.

This study aimed to relook at a small sample set of core plug data and use the latest tight reservoir analytical technology, to see if these techniques might give a better understanding of these rocks, and justify further studies into the reservoir quality and hydrocarbon occurrence. A fundamental question is how the gas flows from the rock to the wells and the relative roles of the matrix, micro-fractures and fractures. The small core plug samples provided were aimed at studying the micro-porosity, permeability and micro-fractures of the matrix mostly at the microscopic level.

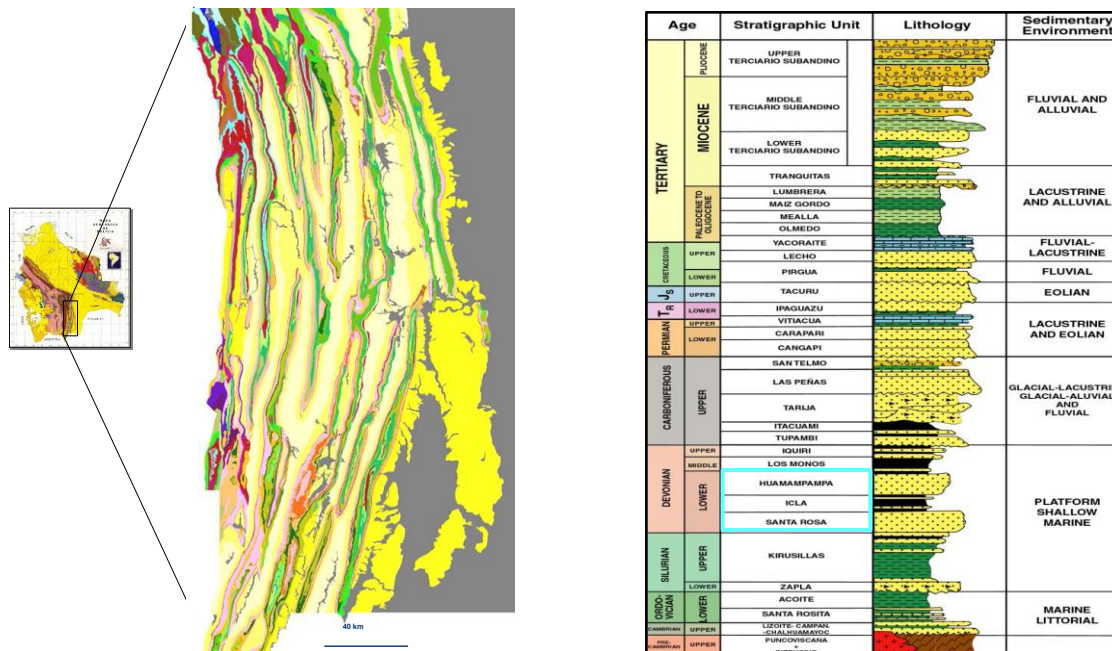


Figure 1: Location Maps for Bolivia, the anticlines hosting the large gas fields, and the Stratigraphic column with the main Huamampampa, Icla and Santa Rosa reservoirs (figures based on Baby et al., 1995; Moretti et al, 2002; Miranda et al, 2003).

2.0 METHODS

The study is based on a small selection of core plugs from each of the five studied fields and the Huamampampa, Icla and Santa Rosa reservoirs. They were taken from 33 cored intervals in 14 wells, using a series of adjacent plugs (70 in total). This means there were only a few samples from each reservoir in each field so that only broad regional or depth trends can be discerned and it is not justified to make detailed inferences about stratigraphic or facies control.

The mineralogy and texture were investigated using a Zeiss Axio Imager M2m auto-mosaic optical imaging system scanner for thin section analysis in the Department of Applied Geology. This was coupled with a TESCAN Integrated Mineral Analyser (TIMA) to automatically map elements, identify grain mineralogy and analyse texture including grain size and pore space all at the nano-scale. This is a SEM-based automated system in the John de Laeter Centre which has four integrated EDS detectors for collection of modal, liberation or bright phase modes, RGB colour cathode-luminescence detection, SE and BSE detectors. The results were compared with transmitted, reflected and fluorescence microscopy (minerals and organic matter) and calibrated with XRD analysis of some samples.

Full Micro CT Imaging acquisition and processing has been done to investigate the very small scale micro-fractures down to 0.6µm in X, Y, Z directions. The micro-CT was coupled with other analyses such as core-plug NMR analysis to reveal the microstructure in three-dimensions and investigate the very small scale micro-porosity and micro-fractures. The MCT measurements were done over small sample areas down to about 1mm diameter at ambient and up to the high pressure in-situ conditions. The standard image has a resolution of 3.5µm³ for a sample of 5-8 mm diameter. The 3D files of the micro-CT images are very large so that movies have been made to allow visualisation by the clients without the need for special software.

Helium porosity and ultra-low Permeameter tests (using the AP-608 Automated Permeameter-Porosimeter from Coretest) were run to obtain poro-perm measurements because routine core analysis of poro-perm was not applicable on these rocks. This apparatus is equipped with a hydrostatic core-holder which can carry out the measurements under net effective pressures. The porosity of the samples is measured using a Boyle's law technique. The porosities and permeabilities were measured using Helium gas as the pore fluid as it is non-toxic, has a high diffusivity and is non-damaging to core samples at pressures up to and over 4000psi.

The NMR analyses were done on samples saturated with 20 g/l KCl brine under 2000 psi hydrostatic pressure, tightly wrapped to prevent water evaporation and moisture absorption, before being placed inside a 2 MHz Magritek Rock Core NMR Analyzer. Transverse relaxation time (T2) experiments were carried out using the Carr-Purcell-Meiboom-Gill sequence (CPMG), the inter-experiment delay was set to 5,000 ms and 20,000 echoes were measured with a τ value at the minimum of 50 µs. The decay was acquired keeping a signal to noise ratio of 200. The raw T2 decay was processed using the 1D inverse Laplace transform, applying the Lawson-Hanson algorithm, for which the T2 distribution is obtained by a non-negative least squares fit.

The mercury injection analyses were undertaken by Dr Ric Daniel at Adelaide University using the Micromeritics Autopore-III porosimeter, which is capable of injecting non-wetting phase (mercury) in user-defined, step-like pressure increments up to 60,000 psi (~413MPa) into an evacuated and cleaned/dried core plug or cut sample. The volume of mercury injected at each pressure increment is automatically recorded until the maximum analytical pressure, or 100% pore-volume Hg saturation is achieved. Pressure is then plotted against incremental Hg saturation readings to generate the drainage curve and the process can be reversed to produce an imbibition curve.

A variety of other analyses were undertaken to better characterize these rocks. These include the Electrical and Elastic Properties so that they can be tied to the log and seismic data and Triaxial strength tests. The purpose of the rock physics tests was to obtain elastic properties of the samples and their dependency on effective stress at in-situ conditions. A confining (radial) stress up to 70MPa is applied by a triaxial (Hoek) cell and axial stress up to 150MPa is applied by a hydraulic actuator. An ultrasonic monitoring system working in shear mode is used to measure compressional (P-wave) and shear (S-wave) wave velocities by implementing the pulse transition method. The equipment comprises an Olympus rectangular form electrical Pulser/Receiver 5077PR, a Tektronix Digital Phosphor Oscilloscope TDS 3034C and a pair of piezoelectric V153 1MHz/.5 transducers (Olympus Panametrics-NDT™). A pair of piezoelectric A114S 1MHz/.75 transducers (Olympus Panametrics-NDT™) working in compressional mode is used as well to double-check the P-wave velocity. All measurements are conducted under room temperature and radial and axial stresses are equal (referred to as confining pressure). The experimental procedure described in Lebedev *et al.* (2013) is used to measure P-wave and S-wave velocities (V_p and V_s respectively). Tri-axial tests have been run by CSIRO to understand the structural and tectonic history and its relation to the diagenesis and low rank metamorphism of the rocks but the results are not reported here.

3.0 RESULTS

A brief summary description is given below of the Curtin results compared only in general terms to existing published and unpublished information (e.g. Baby *et al.*, 1995; Moretti *et al.*, 2002). In general there are few obvious differences in rock quality between the reservoir sandstones in each of the fields or formations. However, the Field B and Field E samples (Table 1) appear to be distinct from samples in Fields A, C and D and there are differences between the Huamampampa, Santa Rosa and Icla reservoirs in terms of their original lithofacies. Mostly the differences are subtle and are over-printed by the deep burial, which has produced relatively high temperature-pressure catagenesis, and by the regional stresses resulting from the late stage thrusting. Together these have destroyed most of the depositional facies control but not all, so that the original or primary porosity has been lost and the associated cementation has stopped the interconnected pore network from preserving primary permeability pathways in many of the samples. The associated formation fluids reacting with the labile bulk rock chemistry have varied in their effects on the development of good connected secondary porosity. In most cases these effects have decreased the connected porosity. However, there are some notable samples where this does not appear to be the case. Nevertheless, the main permeability mechanism seems to result from the fracture network, resulting from the complicated development of the stress fields associated with the thrust folding, which seismic shows has also produced lateral movement and some uplift of the reservoirs to their present depths.

3.1 Sedimentary Lithofacies

The sandstones are all Devonian in age, which is unusual for petroleum reservoirs, deposited mainly in a foreland setting. The Huamampampa and Icla formations are marine or marginal marine whereas the Santa Rosa represents mainly fluvial facies. The cores show that many of these sandstones are significantly bioturbated, which destroyed most of the original sedimentary bedding features and commonly reduces the primary porosity. The organisms that did this were mostly soft-bodied and also leave only minor organic material remains. These sediments were deposited when there was no well-developed land plant cover which means there were no soils and physical weathering of the outcropping rocks dominated rather than chemical weathering. They are mostly or nearly feldspathic litharenites in which the eroded metamorphic and granitic detritus was more able to survive transportation in a near-pristine condition. There is very little land plant organic matter in these sediments, and the TIMA analysis confirmed that most of the fine grained matrix and black laminae commonly described in core reports as organic matter consists mainly of micas, iron oxides and heavy minerals.

3.2 Petrological, Mineralogical and Grainsize Analysis

The sandstones are mainly moderately sorted, very fine to medium grained feldspathic litharenites. They are dominated by quartz, plagioclase and orthoclase feldspar (Table 1 and Figure 2). The thin sections indicate that about 40-60% of the rock occurs as individual quartz grains with an additional 10-30% quartz occurring in composite rock fragment grains, mostly metamorphic grains, but with some granitic igneous rocks fragments. These composite rock fragment grains have no effective internal porosity or permeability unless removed by later catagenesis. That is, where the labile minerals have been corroded by formation fluids to create secondary porosity. Micas are common, including muscovite, illite/muscovite and biotite/chlorite. Framboidal pyrite, iron oxides and other sulphides including rare sphalerite and galena are dispersed through many samples or in the fractures. There are a variety of very small grains or rare minerals such as garnet, zircons, tourmaline, rutile and apatite. Ankerite is a common pore fill commonly precluding all interstitial porosity. These accessory minerals could be used to track the catagenesis, paleo-temperature, age and fluid inclusion history.

Comparison of the TIMA scans in Figures 2, 4 and 5 and the mineral abundances in the Table 1 show there are some significant differences between the samples for the fields and formations. This may be partly due to a lack of sample coverage and is also related to grainsize with more mica and feldspar in the finer samples (Figure 3). Nevertheless there does seem to be more feldspar in Field A (Formation 1) and in Field D, especially in Formation 2 as well as significant differences in the illite/mica occurrence (Table 1 and Figure 2). These differences impact the reservoir quality but in complex ways. For example, the cleaner sandstones probably had better initial primary porosity but are now more cemented whereas the sandstones with more labile clasts (e.g. feldspars) probably had lower

initial primary porosity but subsequently have developed more secondary porosity. Simple cross-plots of Quartz and Mica (illite/mica) content versus Porosity and Permeability produce remarkably good fits to the data even without taking into account grainsize (Figure 3).

Field	FIELD A		FIELD B						FIELD C				FIELD D					
	Formation 1		Formation 1						Fmn 1	Formation 3			Fmn 1	Formation 1		Fmn 2	Fmn 3	Fmn 2
Sample Number	1	8	10	12	14	16	23	24	31	34	37	39	42	47	55	58	62	68
Sample Depth	3130.50	3411.20	4530.30	4531.35	5136.29	5138.15	4110.92	5382.15	4441.67	5571.10	5718.15	5702.10	4448.75	4384.10	4598.65	5332.73	4476.97	4355.55
Minerals / Mass [%]	Sample 1 -	Sample 8 -	Sample 10 -	Sample 12 -	Sample 14 -	Sample 16 -	Sample 23 -	Sample 24 -	Sample 31 -	Sample 34 -	Sample 37 -	Sample 39 -	Sample 42 -	Sample 47 -	Sample 55 -	Sample 58 -	Sample 62 -	Sample 68 -
Quartz	63.52	75.42	83.35	84.57	85.35	88.42	75.42	89.93	90.32	76.46	82.17	86.32	82.11	80.52	74.55	75.57	73.82	87.63
Plagioclase	14.95	13.60	8.70	6.90	6.19	5.77	11.51	4.98	2.42	13.93	8.79	6.81	9.50	9.32	11.95	6.82	4.23	6.13
Orthoclase	4.48	4.30	2.89	2.93	1.79	1.80	4.16	1.35	5.43	1.99	7.20	5.29	6.73	4.88	5.08	4.05	10.66	5.02
Illite/Muscovite	12.06	4.19	3.00	2.90	2.53	2.56	4.82	1.67	1.61	5.56	1.20	1.26	1.32	3.79	6.08	9.71	10.51	0.89
Amphibole/Pyroxene	2.10	1.24	0.74	0.57	0.37	0.34	1.17	0.27	0.07	0.44	0.17	0.14	0.14	0.47	1.21	0.40	0.58	0.10
Ankerite	0.01	0.01	0.56	1.45	3.28	0.76	1.16	1.21	0.00	0.09	0.00	0.00	0.00	0.00	0.04	0.00	0.00	0.06
clinocllore/Biotite	1.19	0.61	0.48	0.46	0.18	0.15	1.18	0.27	0.01	0.32	0.06	0.05	0.04	0.70	0.60	0.68	0.06	0.04
Iron Oxide	0.61	0.09	0.01	0.01	0.02	0.05	0.02	0.05	0.00	0.67	0.00	0.01	0.00	0.05	0.05	1.79	0.01	0.01
Tourmaline	0.27	0.07	0.03	0.03	0.02	0.02	0.09	0.02	0.00	0.06	0.01	0.00	0.01	0.05	0.09	0.55	0.06	0.01
Rutile	0.23	0.14	0.04	0.03	0.04	0.02	0.09	0.04	0.02	0.14	0.02	0.02	0.03	0.06	0.13	0.18	0.03	0.02
The rest	0.58	0.32	0.18	0.17	0.22	0.10	0.37	0.21	0.13	0.33	0.38	0.11	0.10	0.15	0.21	0.25	0.04	0.09
Total	100.00	100.00	100.00	100.00	100.00	100.00	100.00	100.00	100.00	100.00	100.00	100.00	100.00	100.00	100.00	100.00	100.00	100.00

Table 1 TIMA mineralogical analyses confirmed by XRD and thin section.

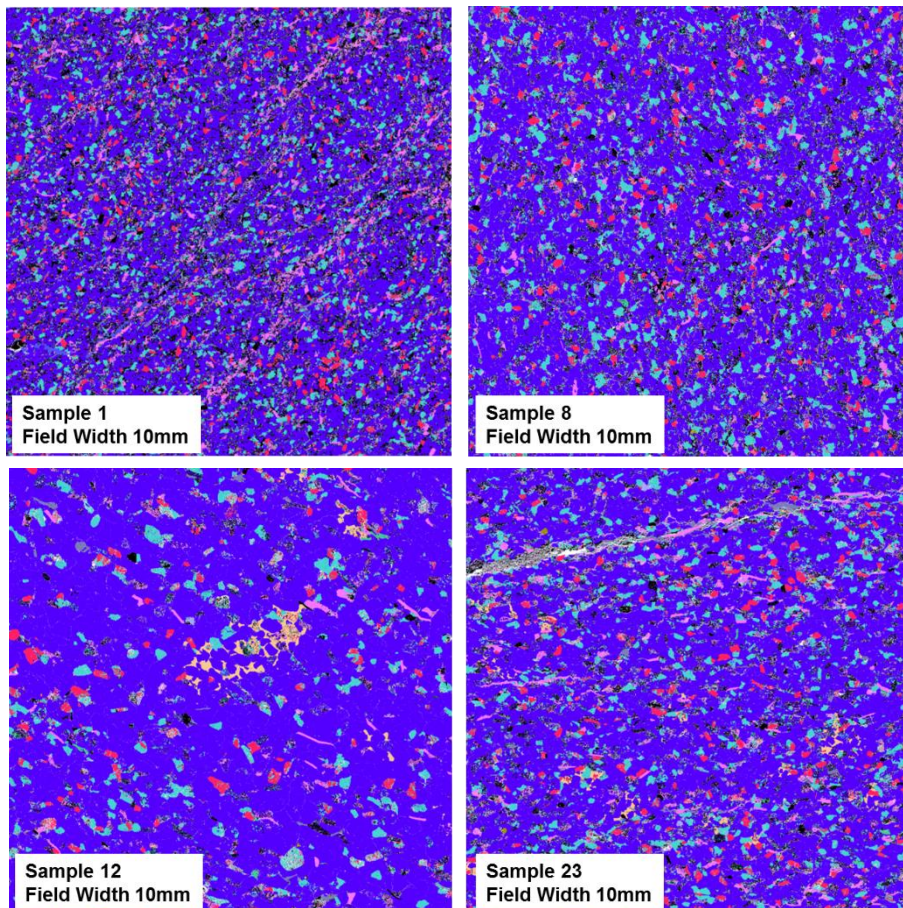


Figure 2: TIMA pan views showing variation in the same formation between Field A and Field B, in terms of compositions (blue quartz, red orthoclase, light blue albite, pink mica), grainsize, textures (note preferred orientation of quartz and micas), fractures, schistosity (top left), porosity (white) and pore fill (orange ankerite and black iron oxides). The large micro-fracture top right in Sample 23 is partially open and partially filled with hematite/magnetite, pyrite and sphalerite or galena.

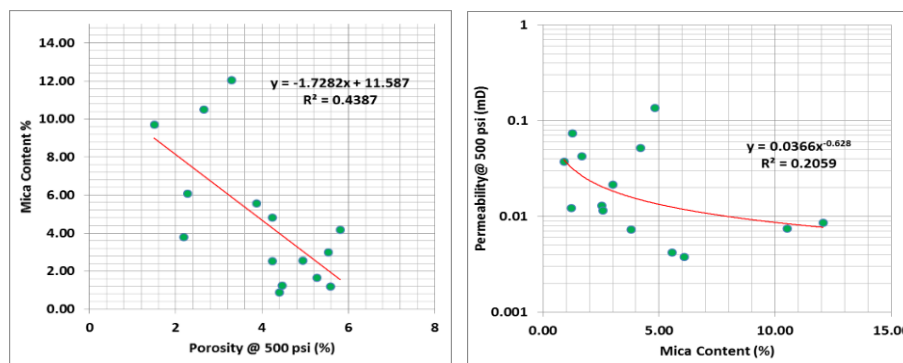


Figure 3: Cross-plots of Quartz and Mica content versus Porosity and Permeability.

Some samples show well-developed nano-scale microporosity around the grains (Figure 5) and this is more common in Formation 1.

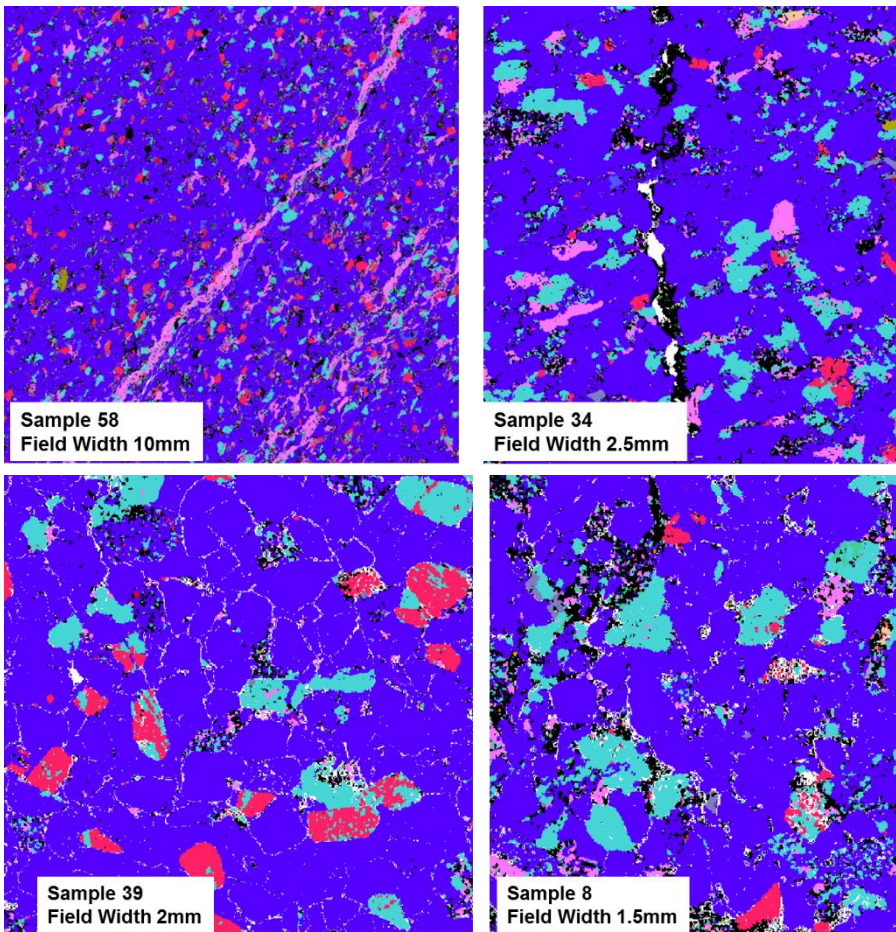


Figure 4: TIMA pan views showing on the left the Field D Formation 3 composition (blue quartz, red orthoclase, light blue albite, pink mica), grainsize, textures (note preferred orientation of quartz and micas), what appear to be quartz filled fractures?, schistosity (note micas on bottom right), virtually no porosity (white) and pore fill (black iron oxides/sulphides). On the right a close-up view of an open fracture (white) which is partially filled with hematite/magnetite. Note this sample has virtually no microporosity around the grains when compared with Figure 5.

Figure 5: TIMA close-up views of the Formation 1 in Field C on the left and in Field A on the right. In both cases nano-scale microporosity can be seen around the grain boundaries and within composite grains (blue quartz, red orthoclase, light blue albite, pink mica), grainsize coarser on the left with equant texture and finer on the right with elongation of the grains and preferred orientation of quartz, pore fill (black iron oxides/sulphides).

3.3 Micro-CT Structural Analysis

The micro-CT analyses are the best indicator of the internal pore structure and micro-fracture network. An example is shown in Figures 6a and 6b for Field B Sample 27, run at very high resolution (0.9814 μm). The void volume fraction was measured as 6.6 %. The figures show the sutured nature of the sand grain boundaries and the pore morphology between grains. They also show areas of secondary sieve-like micropores where the feldspars and other labile grains have been removed. The 3D movies of these micro-CT analyses show that although the secondary dissolution pores are mostly isolated, some large areas containing the grain boundary pores are interconnected in this sample which explains the Hg injection results undertaken on a nearby sample (described later).

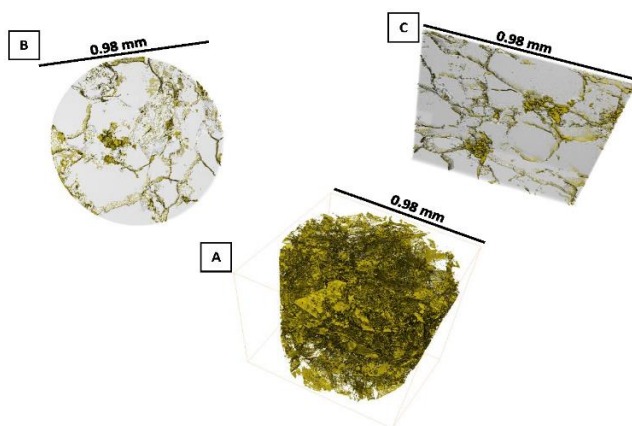


Figure 6a. Field B Sample S27, 0.9814 μm . (A) 3D visualization; (B) horizontal slice and (C) vertical slice through the middle of the sample.

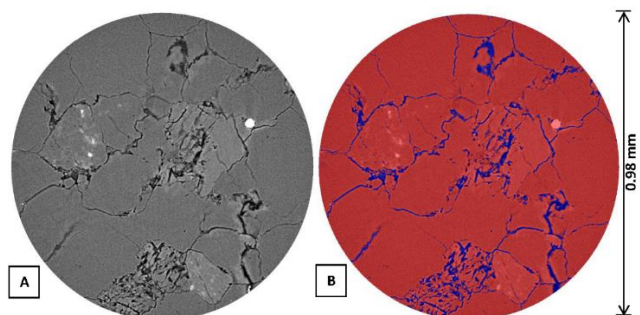


Figure 6b. (A) 2D slice of raw image; (B) segmented image



Another Field B sample had macrofractures that were visible by eye, so it was imaged at medium resolution (10.9 μm voxel size). The 3D movie of this sample showed there are two fractures, which branch or join, both filled with Ankerite which is high density (Figure 7). Some of the much smaller pore spaces are also filled with ankerite. The movies and detailed slices show that the high density minerals have filled most but not all of the fractures which seem to be open in places. The most important point is that the connected micropore network as shown in the sample in Figure 6 should be able to connect to the micro-fractures as shown in Figure 7 for enhanced permeability. The results could be studied with the FracPaQ software to assess the connected porosity and fracture network (Healy *et al.*, 2017).

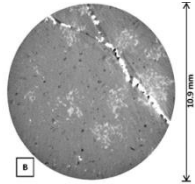


Figure 7. Field B Sample 3D image showing two connected meso-fractures (top left, yellow-orange) in the core plug (still image from a 3D movie). Inset is a horizontal-section through the fractures. Horizontal field width approximately 1cm.

3.4 Helium Porosity and Permeability Analysis

The Helium porosity and permeability results are consistent with previous data for the matrix in these reservoirs (Figure 8). The data indicate the sandstones are tight to ultra-tight with porosities in the range of 2-6% and with permeabilities ranging from just over 0.1mD down to 0.001mD at a confining pressure of 500psi. However, all of the permeabilities reduced significantly when the confining pressures were increased in increments of 500 psi to 4000 psi which is approaching reservoir conditions (Figure 8). At a pressure of 4000 psi the permeability values decrease to less than 0.001mD indicating an ultra-tight reservoir formation. This indicates the microporosity is closed under overburden pressure and the rock loses connected porosity and hence permeability. One plug developed a microfracture in which case the permeability increased substantially (see red dot).

The Field A samples span the range of poro-perm data (samples 2 to 9) whereas the Field B samples tended to have better porosities and permeabilities (samples 11 to 25). The Field C samples also tended to have better porosities but still spanned most of the range in permeabilities (samples 35 to 40). The Field D samples (samples 48 to 67) had the lowest porosities and lowest permeabilities with one exception.

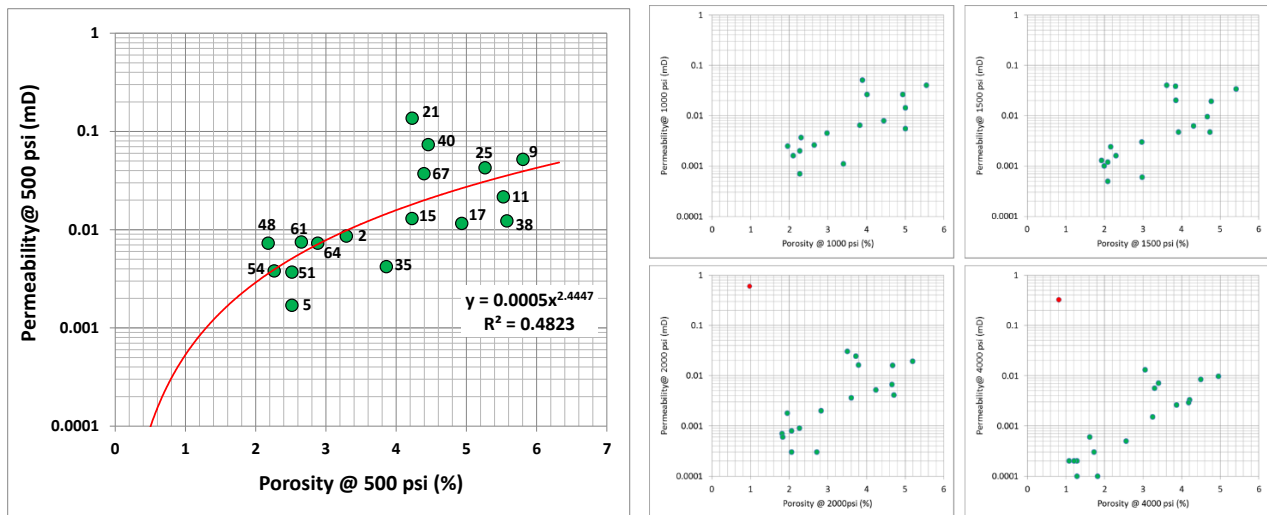


Figure 8 Cross plot of porosity versus permeability measured at 500psi confining pressure on the left, with plots showing the effect of increasing the confining pressures on the right. Most samples analysed are tight or ultra-tight sandstones. At the pressure of 4000 psi the permeability values decrease to less than 0.001mD indicating an ultra-tight reservoir formation. A micro-fracture developed in one of the samples at a confining pressure of 2000 psi (red dot).

Cross plots of Porosity versus Permeability for the Curtin analysed samples together with data from well completion reports are shown in Figures 9 and 10 to place these samples in perspective. The data show that most of the sample poro-perms overlap and this is not obviously related to a field, depth of burial or depositional lithofacies as is commonly the case. There are some differences between some of the fields particularly Field B which appears to have higher porosities.

The most significant difference is between the matrix poro-perm properties and the fracture poro-perm properties. The matrix poro-perm follows a moderately predictable relationship whereas the fracture poro-perms are scattered and presumably related to fracture length and width.

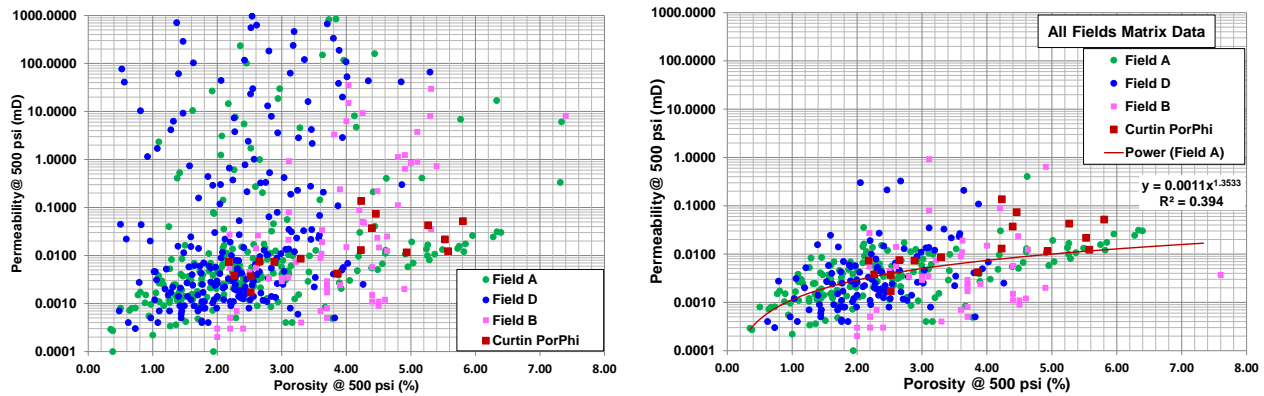


Figure 11: Cross plot of porosity versus permeability for well completion core data from Fields A, B and D and the corresponding Curtin sample data. Matrix and Fractured sample data are plotted together on the left. The Matrix only sample data are given in the plot on the right in which the fitted curve only uses the Field A data.

3.5 NMR Analyses

NMR data was acquired for the seven fully saturated samples covering the range of fields and formations. Their T2 spectra are shown as solid lines in Figure 12. In a brine-saturated rock, the T2 decay spectrum represents a pore-size distribution, with the smallest pores having the highest surface area to volume ratio and therefore shortest T2, and the largest pores having the lowest surface area to volume ratio and therefore the longest T2 relaxation time. The mean peak and dominant T2 time for the samples varies from 10 to more than 100 ms. In most of the cases NMR porosity was slightly less than Core porosity (see the table in Figure 12) probably due to the inability to fully saturate these very tight samples and this was also found with some of the other analyses (e.g. the triaxial tests).

The NMR pore-size distributions show there is a clear distinction between the Formation 1 samples, which have larger pore size distributions (S17, S21, S25 and S40) and the Formation 2 and 3 samples that are much finer grained (S35, S51 and S57). Note this appears the case even within the same fields (e.g. both S40 and S35 occur in the Field C).

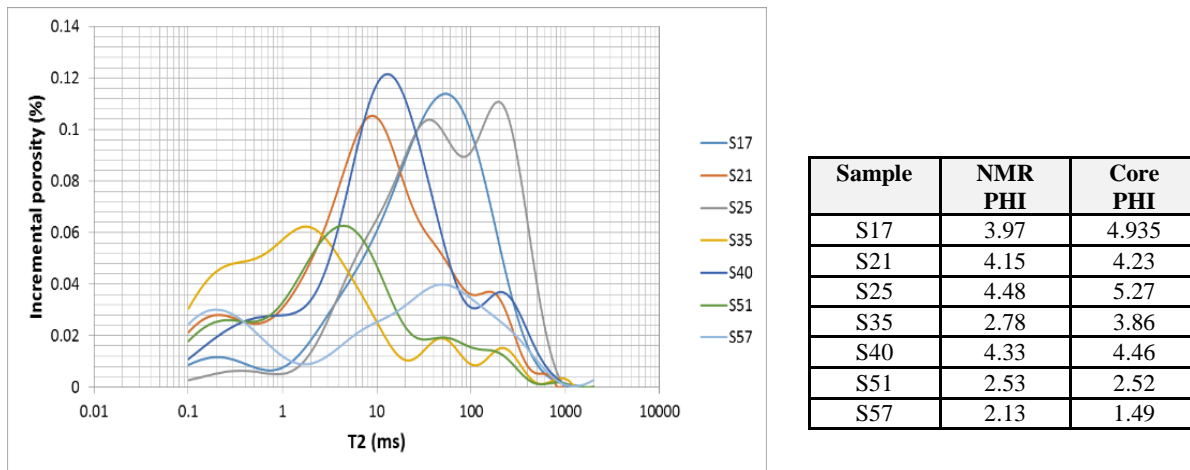


Figure 12: Nuclear magnetic resonance (NMR) T2 relaxation time for the studied samples and derived porosity estimates.

3.6 Mercury Injection Analyses

Hg injection analysis was undertaken on seven of the samples and the results for two are shown in Figure 13. Overall the shape of the injection curves suggest that there are no significant pore throats larger than about 1 micron in diameter, indicated where the curves kick upwards at the threshold pressure point, the point where the mercury starts to migrate significantly into and through the rock. Most samples contain a very fine pore throat network with only a comparatively minor network of pore throats larger than one micron. If there were significant micro fractures or connected secondary pores there should be a kick in the curve at much larger pore throat diameters. The samples are unusual in having low porosity yet relatively low threshold pressures, which probably results from the quartz overgrowths and iron cements or due to some of the late stage minor mineral dissolution.

The data show a variation from sample to sample and they appear to match the trends seen in the pre-existing datasets. The samples can be compared using the two end member examples shown in Figure 13. The Field A sample is the worst quality reservoir sample

with threshold breakover at <0.1micron and only ~30% saturation by a pore throat diameter of ~0.1micron, which is expected given it is a very fine grained sandstone with a high illite/muscovite proportion in the matrix (Figure 13). The Field B samples are the best quality with threshold breakovers at <0.6 micron and with >60% saturation by pore throat diameters of ~0.1micron. The Field C sample has a threshold breakover at <0.4micron and has >40% saturation by pore throat diameters of ~0.1micron. The three Field D samples vary with grainsize and porosity, having a threshold breakover at <0.3-0.2 micron and >10-30% saturation by pore throat diameters of ~0.1micron, and overall are not as good as the Field B or Field C samples but are better than the Field A sample.

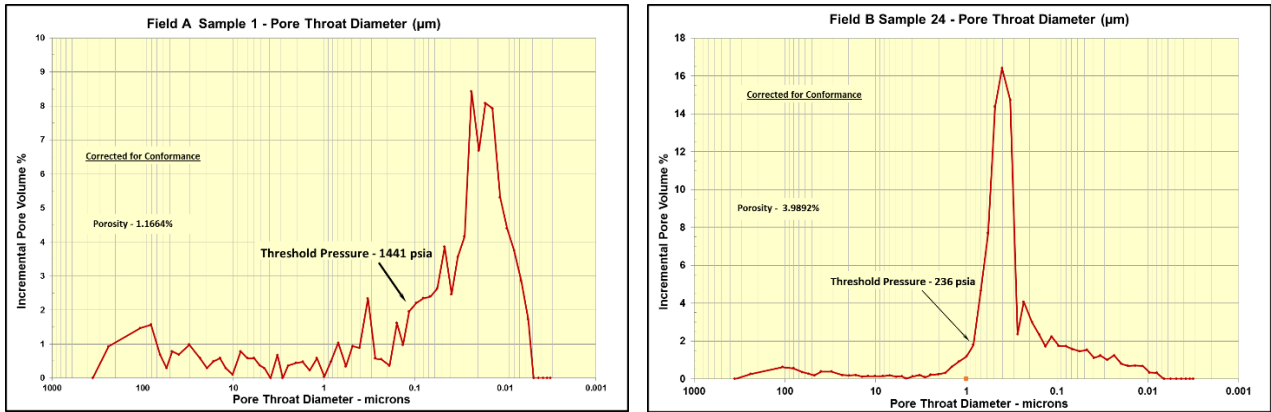


Figure 13: Mercury Injection Capillary Pressure curve converted to Pore Throat Diameter (microns) for Field A (Sample 1) and Field B (Sample 24).

3.7 Elastic Properties

The measurements of the P- and S-wave velocities were done for a small subset of dry samples under room pressure and temperature, being extended on one sample to measure velocities versus a series of increasing effective pressures. The results of these tests can be used to tie the results to the logs and seismic datasets for log analysis, velocity, anisotropy, AVO, inversion or 4D seismic analysis. Measurements of the S-wave velocities polarized in perpendicular directions showed that the samples are slightly anisotropic. They have unusually high P-wave velocities for reservoir sandstones commensurate with their deep burial and induration (Figure 14). There is a weak trend with depth within a field but not between fields probably due to their variable thrusting and uplift histories. The Field A Sample 3 was analysed at several effective pressures because it appeared to contain minute fractures. The results showed that there was a significant stress dependency with velocities as we expected. This is a clear indication that fractures exist within this sample and that similar fractures in the reservoir would affect any seismic data. The measured strength and stress dependency was abnormally high for reservoir sandstones compared to most reservoirs sampled from shallower depths that exhibit less strength.

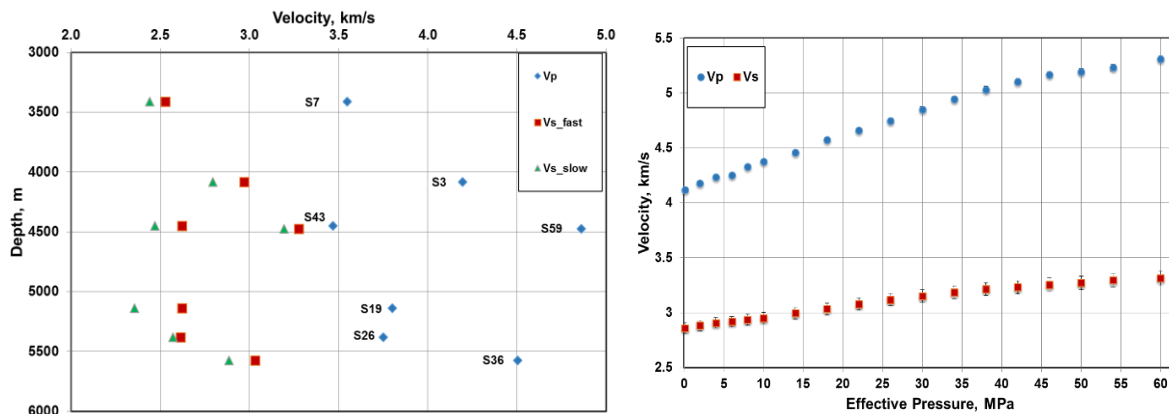


Figure 14: P- and S-wave velocities plotted against depth (left) and against effective pressure (right).

4.0 CONCLUSIONS

The samples are all very tight sandstones and there are few obvious differences in their reservoir quality across fields or formations. However, the Field B and Field E samples appear to be distinct from the Field A, C and D samples and there are subtle differences between the samples for each reservoir formation. Mostly the differences are over-printed by the deep burial, which has produced relatively high temperature-pressure catagenesis, and by the regional stresses resulting from the late stage thrusting. Together these have destroyed most of the depositional facies control but not all, so that the original or primary porosity has been lost and the associated cementation has stopped development of a good interconnected secondary pore network in most cases. However, there are some notable samples where a grain boundary microporosity exists and where dissolution of grains has produced some secondary porosity. Hence, some samples such as from Field B, have slightly higher porosities and the micro-porosity may be connected to the micro-fractures.

Nevertheless, the main permeability mechanism results from the fracture network, resulting from the complicated development of the stress fields associated with the thrust folding. This means the biggest difference is between the matrix poro-perm and the fracture poro-perm. The above conclusions are consistent across the range of datasets, including the TIMA photomicrographs, the micro-CT data, plots of porosity versus permeability, NMR and mercury injection pore size distributions.

The main observations about these core samples based on the analyses can be summarised as:

- The samples are mostly ultra-tight feldspathic litharenites composed of quartz, feldspars and clay/micas but much of the quartz is in metamorphic or igneous rock fragments that originally had no internal porosity or permeability.
- Significant burial and regional orogenic low T-P catagenesis has compacted, welded and metamorphosed most minerals producing a fissile, almost schistose fabric with quartz cementation and clay to mica transformations.
- Subtle but significant differences exist between the fields and the reservoirs that are controlled by depositional facies, burial catagenesis and structuring. Together these control the microporosity and matrix permeability.
- The porosity is low typically 0.5-7% with very low matrix permeabilities (typically 0.0001-1mD) but much higher fracture permeabilities up to 1Darcy or more.
- The primary porosity has been mostly cemented by quartz, ankerite, illite/mica and iron oxides/sulphides.
- The remaining matrix porosity is mostly <1micron and the permeability reduces by a factor of 10 at in-situ pressures.
- The microporosity can be seen on the micro-CT and TIMA-SEM images as a very fine <1micron pores around the large grains and at the corner points and in some samples is available to connect to the micro-fracture network.
- Secondary microporosity occurs as micropores between grains or within the more labile minerals such as feldspars but is not commonly connected to microfractures.
- Most samples do not show good micropore and microfracture connectivity.
- However, some samples do appear to show connectivity or potential for connectivity to the meso-fracture network.
- The rocks have cemented micro-fractures and more recent open microfractures, though these may be shut at in situ pressures.
- Hydrocarbon storage should be possible in some of the primary microporosity, the secondary microporosity and the open micro-fractures provided that the entry pressures allow.
- Significant production of hydrocarbons and water movement between the matrix and fracture network is doubtful in most reservoir units but may be possible in others.

ACKNOWLEDGMENTS

The Curtin authors would like to acknowledge the opportunity to work on these fascinating and challenging reservoirs provided by 3d-Geo and the support they provided throughout the studies. Curtin and CSIRO support staff and doctorate students who have worked on these samples include Kelly Merigot, Mark Aylmore and Veronica Avery in the John de Laeter centre; Nadia Testamanti and Dr Mohammad Sarmadivaleh in Petroleum Engineering; Andrew Wiczorek in Applied Geology; Dr David Dewhurst and the Rock Mechanics team in CSIRO Perth. These studies have been supported by the Curtin University facilities and staff especially those in Applied Geology, the John de Laeter Centre and Petroleum Engineering. Dr Ric Daniel at Adelaide University competently carried out the mercury injection analyses. The conclusions and views expressed are those entirely of the authors.

REFERENCES

- Baby, P., I. Moretti, B. Guillier, R. Limachi, E. Mendez, J. Oller and M. Specht, 1995, Petroleum system of the northern and central Bolivian sub-Andean zone, *in* A. J. Tankard, R. Sukrez S. and H. J. Welsink, Petroleum Basins of South America: AAPG Memoir 62, p. 445-458.
- Florez-Nino, J, Aydin, A., Mavko, G., Antonellini, M. and Ayaviri, A., 2005, Fault and fracture systems in a fold and thrust belt: an example from Bolivia. AAPG Bulletin, 89, 4, 471-493.
- Healy, D., Rizzo, R. E., Cornwell, D.G., Farrell, N. J.C, Watkins, H., Timms, N.E., Gomez-Rivasa, E., Smith, M., 2017, FracPaQ: A MATLAB™ toolbox for the quantification of fracture patterns. Journal of Structural Geology 95, 1-16.
- Lebedev, M., Pervukhina, M., Mikhaltsevitch, V., Dance, T., Bilenko, O., and Gurevich, B., 2013, An experimental study of acoustic responses on the injection of supercritical CO₂ into sandstones from the Otway Basin. Geophysics, 78, 4, D293-D306.
- Miranda, A.P., Souza Cruz, C.E., Melo, J.H.G. and Oller, J., 2003, Sequence Stratigraphy of the Late Silurian – Devonian Subandean Basin in Southern Bolivia & Northern Argentina. ACGGP VIII Simposio Bolivariano - Exploracion Petrolera en las Cuencas Subandinas.
- Moretti, I., Baby, P., Mendez, E. and Zubieta, D., 1996, Hydrocarbon generation in relation to thrusting in the Sub Andean Zone from 18 to 22°S, Bolivia. Petroleum Geoscience, 2, 17-28.
- Moretti, I., Labaume, P., Sheppard, S.M.F. and Boulegued, J., 2002, Compartmentalisation of fluid migration pathways in the sub-Andean Zone, Bolivia. Tectonophysics 348, 5-24.